

The illumination angle dependency of CPV solar cell electrical performance



L.A.A. Bunthof*, J. Bos-Coenraad, W.H.M. Corbeek, E. Vlieg, J.J. Schermer

Radboud University, Institute for Molecules and Materials, Applied Materials Science, Heyendaalseweg 135, 6525 AJ Nijmegen, The Netherlands

ARTICLE INFO

Article history:

Received 4 November 2016

Received in revised form 9 January 2017

Accepted 11 January 2017

Available online 19 January 2017

Keywords:

CPV

Optics

Angle of illumination

Front metal grid

Ray tracing

ABSTRACT

CPV systems aim to deliver electrical power at lower cost than will be possible with traditional photovoltaics. To achieve this, maximum performance from the solar cells should be obtained, while minimizing the cost of balance-of-system. Therefore it is important that CPV optical systems are evaluated in terms of their impact on solar cell performance. One attribute of particularly lens based CPV systems is the variance in incidence angles of light at the solar cell surface, especially when a secondary optic element is employed. The electrical performance of TJ CPV solar cells for varying angles of incident illumination is studied in detail. The solar cells suffer a loss of performance of up to 58% for oblique illumination. Calculations and ray tracing simulations show that optical losses are caused by Fresnel reflections off the ARC, and scattered reflections off the front metal grid due to surface roughness. Additionally the merit of using secondary optics in spite of this effect is shown for symmetrical CPV systems. For asymmetrical (i.e. prism based) systems however, the loss of performance may be substantially larger. Therefore grid orientation and design in respect to the optical system should be taken into account and optimized in such systems.

© 2017 The Authors. Published by Elsevier Ltd. This is an open access article under the CC BY license (<http://creativecommons.org/licenses/by/4.0/>).

1. Introduction

Concentrated photovoltaic (CPV) systems aim to deliver electrical power at a lower cost than will be possible with traditional photovoltaics (Swanson, 2000; Baharoon et al., 2015). To achieve this goal, maximum performance from the multijunction solar cells optimized for concentrators should be obtained, while minimizing the cost of optics, temperature control and other balance-of-system (Antón et al., 2003). As efficiency limits for 3-, 4- and more junction III-V CPV cells continue to rise (NREL, 2016) the chances for economically viable CPV systems are increasing, yet this also puts more demands on the concentrating systems. Therefore it is important that these optical systems are evaluated in terms of their impact on the solar cell performance (Herrero et al., 2012; Rodrigo et al., 2013; Kinsey et al., 2008; Or and Appelbaum, 2014). One attribute of in particular lens based CPV systems is the variance in incidence angles of light at the solar cell surface. Another important concern is inhomogeneity of the light distribution on the cell introduced by the optical system (Garcia et al., 2008; Fernández et al., 2011; Espinet González et al., 2012; Martin et al., 2015). This may cause loss of performance due to

an increased series resistance, as well as current mismatch between junctions (James, 1994). Therefore, many concentrator system designs aim to minimize this inhomogeneity by means of a homogenizing Secondary Optical Element (SOE) (Benitez and Miñano, 2003; Schmid et al., 2014). SOEs can reduce spatial and spectral inhomogeneity via (multiple) internal reflections of the incident light. In addition, a SOE usually adds secondary concentration to a CPV system. However, while the performance is increased and the irradiance homogenized, in general the average angle of incidence (AOI) on the cell surface also increases further as illustrated in Fig. 5. As solar cells are typically optimized for use with near-perpendicular illumination, CPV cells - especially in conjunction with a SOE - will suffer from loss of performance by the AOI variance caused by the optics. For instance the Anti Reflection Coating (ARC) may show an angular dependency, but also the exact form and orientation of the front contact grid fingers will have an increasing impact on cell performance as the average AOI increases.

Current CPV systems mostly utilize high efficiency InGaP/GaInAs/Ge solar cells with a grid contact for optimal performance under perpendicularly incident light. The surface coverage by the grid is kept as low as possible, yet typically up to 10% to minimize resistive losses. The contact lines are also quite high in the order of 5–6 µm for the same reason. Under oblique AOIs however, a high

* Corresponding author.

E-mail address: L.Bunthof@science.ru.nl (L.A.A. Bunthof).

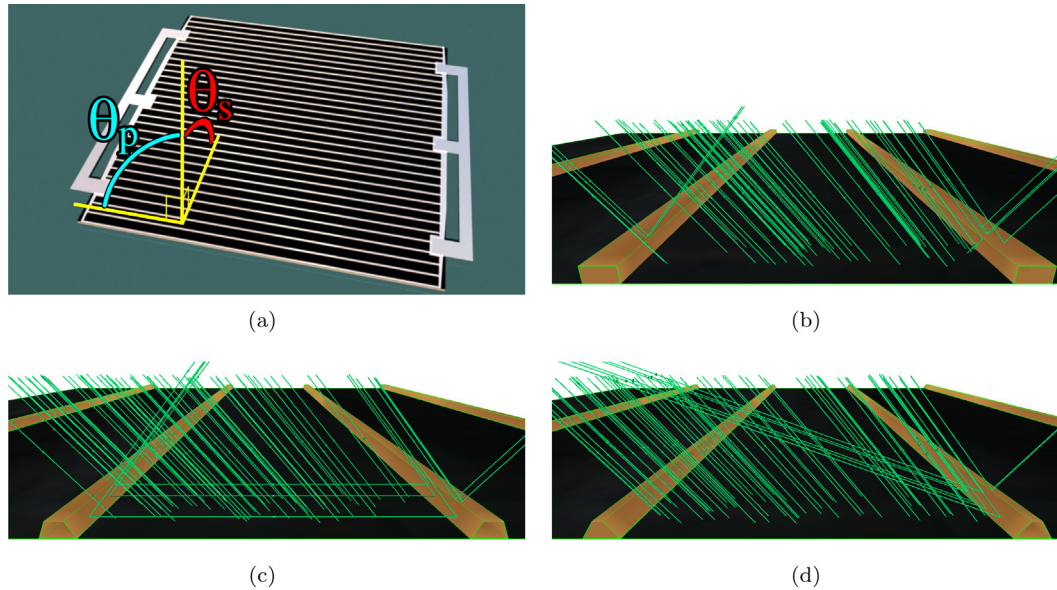


Fig. 1. (a) Schematic representation of the device under test. The cell surface with front grid metallization and contact tabs. Note that the image is not to scale. The parallel (θ_p) and the orthogonal (θ_s) incident angles are shown. Figures (b), (c) and (d) are 3D simulation exports that illustrate grid finger slopes of resp. 90°, 65° and 55° and a light source incident angle of 27°. The brightness gradients of the lines show the trace direction in between surface interactions. Photons travel from dark towards bright.

aspect ratio becomes a disadvantage as the grid lines will increasingly block the light.

In this paper the impact of oblique illumination on CPV solar cell performance is studied in detail. Previous work into this angular dependence has been dedicated to the optical coupling differences between junctions as a function of AOI and temperature (Garcia-Linares et al., 2014). Here we study the total electrical output of CPV solar cells as a function of the AOI, and also the lateral direction of illumination as explained in Section 2.1. Additionally the optical benefits of using a SOE are investigated. Finally the optical benefit of employing a SOE and the hinderance in electrical power generation caused by it are evaluated. For this purpose generally applied square InGaP/GaAs/Ge solar cells with unidirectional front contact grid lines are used. The AOI of incident illumination is varied along two directions - parallel to the grid lines, and orthogonal to it - in order to decompose several causes of cell performance loss. Additionally, 3D ray tracing simulations are performed to study the effects of geometrical light reflections at the grid metal, as well as to study the AOI distributions caused by three different secondary optical elements.

2. Theory

2.1. Definition of incident angles

The AOI of light on the solar cell surface is described here using a spherical coordinate system based on the *zenith angle* θ , and the *azimuth angle* φ . Due to the influence of the grid line shape and orientation, the cell performance will not only depend on θ but also increasingly on φ for more oblique illumination.

In this work, the influence of the azimuth angle φ on the cell performance is investigated by considering the AOIs in the two most distinctive planes across the cell. Firstly the plane that propagates in parallel direction to the grid lines (where $\varphi = \varphi_p$) is considered. In this plane the metal grid will not cause additional reflections or shading for any θ compared to normal incidence. Secondly the plane that propagates in orthogonal direction to the grid lines (where $\varphi = \varphi_s$, from the German *senkrecht*) is considered. In this case, any influence of the metal grid on the cell performance

will be maximal. Zenith angles will be labeled θ_p and θ_s , denoting the plane in which the AOI is varied. This is further illustrated in Fig. 1a.

2.2. Metal grid reflections

For increasing θ_s an increasing fraction of the incident light will interact with the sides of the metal grid, as illustrated in Fig. 2, potentially preventing it from reaching the semiconductor surface. Only if the sides of the grid fingers behave as perfect mirrors and are inclined perpendicular to the cell surface, can cell performance for the orientations θ_p and θ_s be expected to be equal for equal AOI, as the light would in this case simply reflect at the grid metal and reach the solar cell surface under the same angle as the directly incident light (Fig. 1b). If the sidewalls are not perpendicular to the cell surface, a fraction of incident light will reach the cell at different AOI, as shown in Fig. 1c and d.

Fig. 2 shows a schematic cross-sections of a grid finger with side walls inclined under an angle γ with the cell surface. The blue¹ arrows coming from the top represent the parallel incident light which is divided into four fractions: light that makes it to the underlying solar cell directly (L_s), light reflecting on the top of the grid finger (L_t), the light reflecting on the front side of the grid finger (L_α) and, when present light reflecting on the back side of the grid finger (L_β), analogous to L_α . The lowercase fractions l_i are the virtual projections of L_i on the solar cell plane such that $L_i = l_i \cos \theta_s$, for any fraction i . When $\theta_s \leq 90 - \gamma$, incident light is reflected on both sides of the grid finger towards the solar cell surface at angles α and β with the surface. However when $\theta_s \geq 90 - \gamma$, a shadow is cast on the solar cell by the grid finger, represented by the difference $l_\theta - l_\gamma$, decreasing the size of l_s .

Also, in practice these side walls will be rough on a micrometer scale depending on the technologies applied to deposit the metal contact and/or define the lateral dimensions of the grid fingers. As a result, part of the light incident on the side walls will scatter away from the cell as illustrated in Fig. 3.

¹ For interpretation of color in Fig. 2, the reader is referred to the web version of this article.

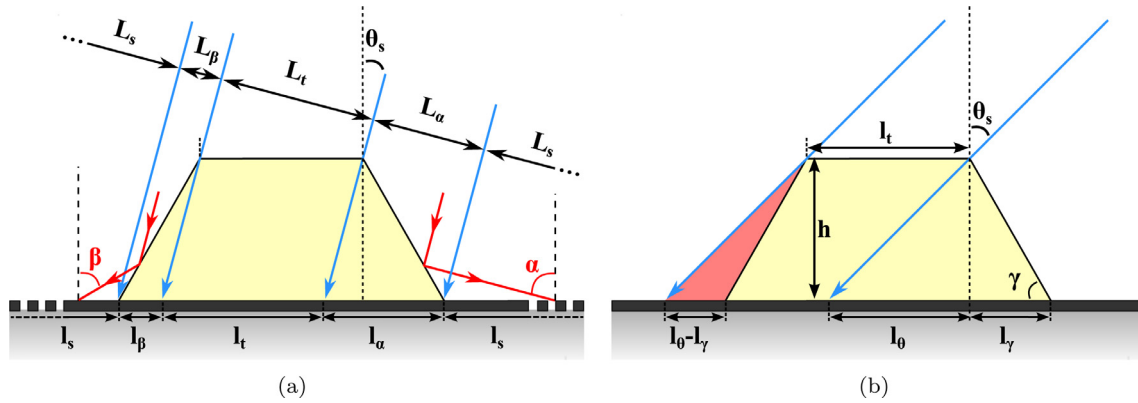


Fig. 2. Cross-section of a grid finger with an incident light beam under angle θ_s . For the analyses the beam of light is divided into four fractions (L_s , L_β , L_t and L_α) and also the cell surface is divided in a number of fractions (l_s , l_β , l_γ , l_0 , l_t , and l_s) that are defined in the figures, together with a number of geometrical parameters that determine the shape of the grid finger (l_t , h and γ).

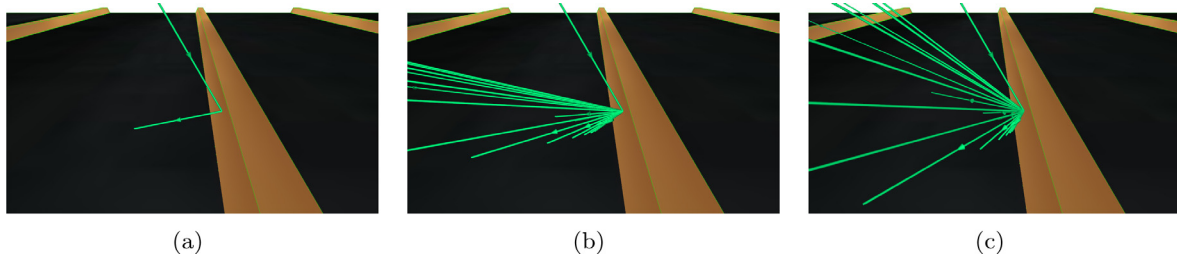


Fig. 3. Roughness/scattering simulations. Surface roughness is assumed to cause scattered reflection of incident photons. Upon reflection at the grid finger, the surface normal is virtually altered with a fixed angle of 5° (a), 15° (b) and 25° (c) in a random direction. To illustrate the ‘conical scattering’, a set of several reflecting photons is drawn on each image. In the performed simulations, a single photon is reflected into a single random direction on the edge of the cone – never within.

2.3. Short circuit current densities for oblique irradiation

With the increase of θ , the irradiance E_e on a tilted solar cell diminishes with $\cos \theta$ where E_0 is the benchmark one-sun irradiation density of 1000 W/m^2 at $\theta = 0^\circ$:

$$E_e(\theta) = E_0 \cos \theta \quad (1)$$

As a first order approach, the short circuit current density J_{SC} is commonly presented as proportional to E_e :

$$J_{SC} = C E_e \quad (2)$$

where C is a constant which depends on the light spectrum and the external quantum efficiency (EQE) of the solar cell. This study demonstrates however, that variations in $J_{SC}(\theta)$ cannot be explained solely by resulting variations in $E_e(\theta)$ i.e. $\frac{dC}{d\theta} \neq 0$.

When observing C on the level of spectral irradiance (i.e., the irradiance per wavelength, $\frac{dE_e(\lambda)}{d\lambda}$), and including the AOI of incident illumination, it can be shown that:

$$C(\lambda, \theta) = \frac{e \lambda \text{EQE}(\lambda, \theta)}{h c} \frac{dE_e(\lambda)}{d\lambda} \quad (3)$$

with e the elementary charge, c the speed of light, and h the Planck constant. Here, incident irradiation density is translated into photon flux via division by the photon energy ($\frac{h c}{\lambda}$). Substitution and integration over the spectrum of light yields an expression for J_{SC} as a function of θ :

$$J_{SC}(\theta) = C(\theta) E_e(\theta) = \frac{e \cos \theta}{h c} \int_{\text{Spectrum}} \lambda \text{EQE}(\lambda, \theta) \frac{dE_0(\lambda)}{d\lambda} d\lambda \quad (4)$$

In this study the angular dependency of J_{SC} caused by other factors than E_e is studied using J-V measurements for oblique incident light both parallel and orthogonal the front contact metal grid. In

this way any influence of the metal grid on the current generation of the solar cells is decomposed from effects caused by the epitaxial cell structure and ARC. To account for the decreasing illumination at the cell surface under inclined angles, all measured data is normalized to $J_{SC}(0) \cdot \cos \theta$ via:

$$N_{J_{SC}}(\theta) = \frac{J_{SC}(\theta)}{J_{SC}(0) \cdot \cos \theta} \quad (5)$$

Additionally, the transmission through the ARC (the applied ARC will be described in Section 3.1) T_{ARC} , will diminish for increasing AOI. This parameter is calculated here based on the Fresnel equations for refraction of light, while interference effects are neglected, as they will have a minor impact. Again, these values are normalized to $T_{ARC}(0) \cdot \cos \theta$ via:

$$N_{T_{ARC}}(\theta) = \frac{T_{ARC}(\theta)}{T_{ARC}(0) \cdot \cos \theta} \quad (6)$$

Because $N_{J_{SC}}$ and $N_{T_{ARC}}$ both represent a measure for the light entering the solar cell, they can be directly correlated to one another as long as $IQE(\theta) = IQE(0)$.

3. Experimental

3.1. Concentrator solar cell structure

In this study, the solar cells under test are $14.9 \times 15.3 \text{ mm}^2$ InGaP/GaInAs/Ge CPV solar cell assemblies, equipped with an ARC for use with glass SOE and front contact metal tabs, produced by AzurSpace. The cells feature silver front grid contact (see Fig. 1a) with fingers having inclined sides as is shown in the SEM image in Fig. 4. An average top width of $6 \mu\text{m}$, an average base width of $11 \mu\text{m}$ and an average height of $5.7 \mu\text{m}$ as was measured using

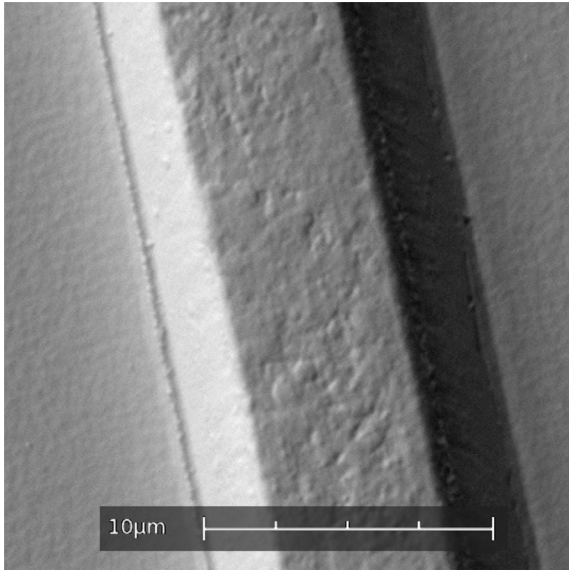


Fig. 4. SEM image of one grid finger of the device under test. The inclined sides of the finger are visible. From SEM and optical microscopy images it is determined that average dimensions for the fingers are: $topwidth = 6 \mu m$, $basewidth = 11 \mu m$, $height = 5.7 \mu m$, which makes the incline angle $\gamma = 66.3^\circ$.

optical microscopy. The heart-to-heart distance of the fingers is $125 \mu m$ and the surface coverage by the grid is 8.8% excluding the busbars.

For uncoated solar cells, the transmittance of incident photons to the semiconductor material is heavily dependent on the AOI. A cell equipped with an ARC will show a different transmission curve, but generally these cells also show increased reflections at oblique AOI. The applied ARC on the studied cells consists of $65 \text{ nm Al}_2\text{O}_3$ on 50 nm TiO_x .²

3.2. Electrical characterization

J-V characterization of the solar cells is performed using an ABET technologies Sun 2000 Class A solar simulator, which provides homogeneous, parallel illumination over a $100 \times 100 \text{ mm}^2$ area. An Ushio 550 W Xenon short arc lamp is used to approximate the AM1.5 spectrum. The setup is equipped with a Keithley 2401 sourcemeter and data acquisition is performed using ReRa Tracer3 software. The J-V curves of three cells have been measured in duplicate for AOI of $0\text{--}83^\circ$. The AOI is modified by pivoting the cell along the θ_p and θ_s orientations, the resp. angles quantified using a digital level with an error margin of 0.1° . During measurement, the solar cell is kept at 25°C by water cooling.

3.3. Geometrical grid finger analysis

As will be shown in Section 4.1, the AOI dependency of current generation is non-identical for θ_p and θ_s orientations. This difference must be explained by the orientation and geometry of the front metal grid.

The ratio of the different fractions of light L_i and I_i (as defined in Section 2.2 and Fig. 2) is evaluated analytically for each θ . Also the incidence angles of light for fractions L_α and L_β on the cell surface

will differ from that of L_s for most θ due to the inclined sides of the grid finger; these angles are also determined. The experimental data from $J_{sc}(\theta_p)$ is used to determine $EQE(\theta)$ at the semiconductor surface, accepting/neglecting the minor error caused at the $J_{sc}(\theta_p)$ measurements for the fractions L_α and L_β (at 2.13% each), where the AOI at the semiconductor surface is larger than that of the vast direct fraction, L_s .

Upon reflection at the grid finger, as a result of surface roughness, diffusion or reflective scattering may occur (Welford, 1977). For that reason, in addition to the analytical calculation, 3D ray tracing simulations are performed using Scientrace ray tracing software³ that allow the inclusion of reflective scattering at the grid finger surfaces.⁴ In these simulations, upon reflection at the surface, the surface normal about which reflection occurs is virtually modified with a static angle in a random direction determining the reflected direction. Note that changing the surface normal with angle $\Delta\psi$ results in a possibility cone with a side-to-side angle of $4\Delta\psi$. Typical reflection alterations are illustrated in Fig. 3.

3.4. SOE concentrator models

Common examples of SOEs are based on external reflection at coated surfaces (Jaus et al., 2009) or refraction (James, 1989; Benitez et al., 2010), sometimes combined with full internal reflection (Victoria et al., 2009), using transparent dielectrics. A basic configuration, as illustrated in Fig. 5a, is simulated to study the effects of refractive SOEs on the distribution of incident angles at the solar cell. A PMMA (Appendix A.1) Fresnel lens with a $40 \times 40 \text{ mm}^2$ square surface and a focal distance of 80 mm is simulated as a primary optic. The simulated SOEs are given the optical properties of standard BK7 glass, further detailed in Appendix A.2.

The SOE shown in Fig. 5b is a truncated pyramid (TP). This is an example of a kaleidoscope-type glass SOE or F-RTP system as described by Mohedano and Leutz (2016). The top and bottom squares are resp. $6 \times 6 \text{ mm}^2$ and $2 \times 2 \text{ mm}^2$. The height of the pyramid is 10 mm.

The base of the Double Truncated Pyramid (DTP), as shown in Fig. 5c is equal to that of the TP SOE, but on top a second, shorter, truncated pyramid is adjoined. The top and bottom squares of this second pyramid are resp. $2 \times 2 \text{ mm}^2$ and $6 \times 6 \text{ mm}^2$, but the height of this top truncated pyramid is only 0.4 mm. This geometry creates an angle of 90° between the adjoining sides of the two pyramids, adding additional concentration by refraction to the basic TP shape as the edges normals are now directed at the cell center. For a quantitative comparison of incident angles at the cell, the reference setup shown in Fig. 5d has only a glass flat plate (FP) with the same optical properties as the TP and the DTP SOEs. In all setups, the focal point of the Fresnel lens is aimed at the topmost surface of the SOE.

3.5. SOE ray tracing

The PMMA Fresnel lens used to simulate the optical efficiency of the different COE configurations described above, is made up of 128 Fresnel planoconvex rings. The flat side of the lens points towards the light source. 'Aspheric-like lens behavior' is obtained in the simulations by using spherical Fresnel rings with a radius optimized for each ring.

The refractive properties of the PMMA cause the focal point of the lens to be wavelength dependent. The defined focal distance

² AlO_x and TiO_x have refractive indices of $n_{\text{AlO}_x} \approx 1.4\text{--}1.6$ (Fiore et al., 1998), Dumeige et al. (2002) and $n_{\text{TiO}_x} \approx 3$ respectively, according to SOPRA data. Based on partial reflections on the ARC layers as described by the Fresnel equations, neglecting the minor fraction of reflections at the top subcell (InGaP), a close match between calculation and experimental data is achieved.

³ An open source, programmable, 3D geometric ray tracing application developed at Radboud University. Available online at <http://scientrace.org/>.

⁴ The Scientrace ray tracing source files used in this study can be downloaded from https://github.com/JoepBC/scientrace/tree/master/example_simulations/aoi_study_simulations.

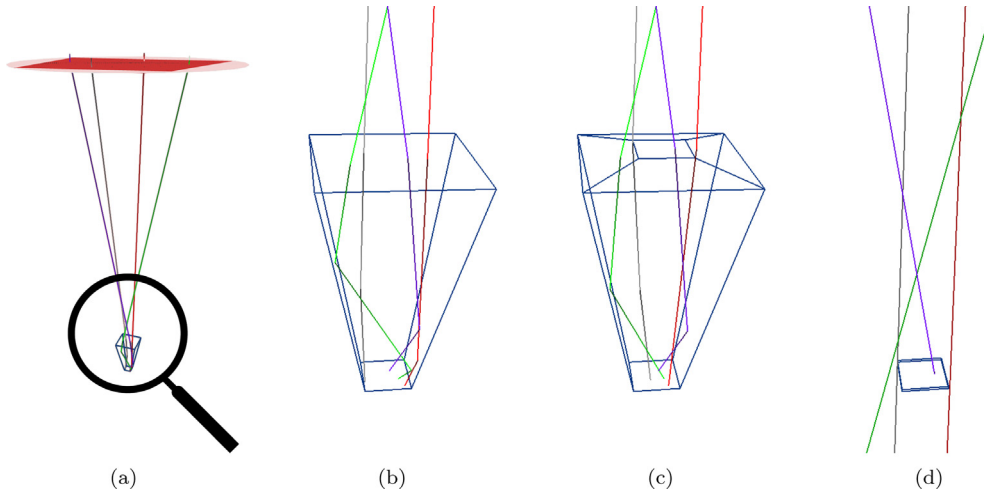


Fig. 5. Secondary optics models overview. All images show the same four traces with their distinct colors. A square Fresnel lens, the bold red area in figure (a), projects the incident light at the top entrance of a BK7 glass SOE. The *Truncated Pyramid* (TP) in (b) has a flat top, whereas the *Double Truncated Pyramid* (DTP) in (c) has the same base structure, but is extended with a second short truncated pyramid on its top. The flat plate (FP) in (d) is added to the plain cell for comparison with the TP and TPD SOEs. The FP SOE does not increase the optical concentration, but it does alter the incident angle at the cell. (For interpretation of the references to color in this figure legend, the reader is referred to the web version of this article.)

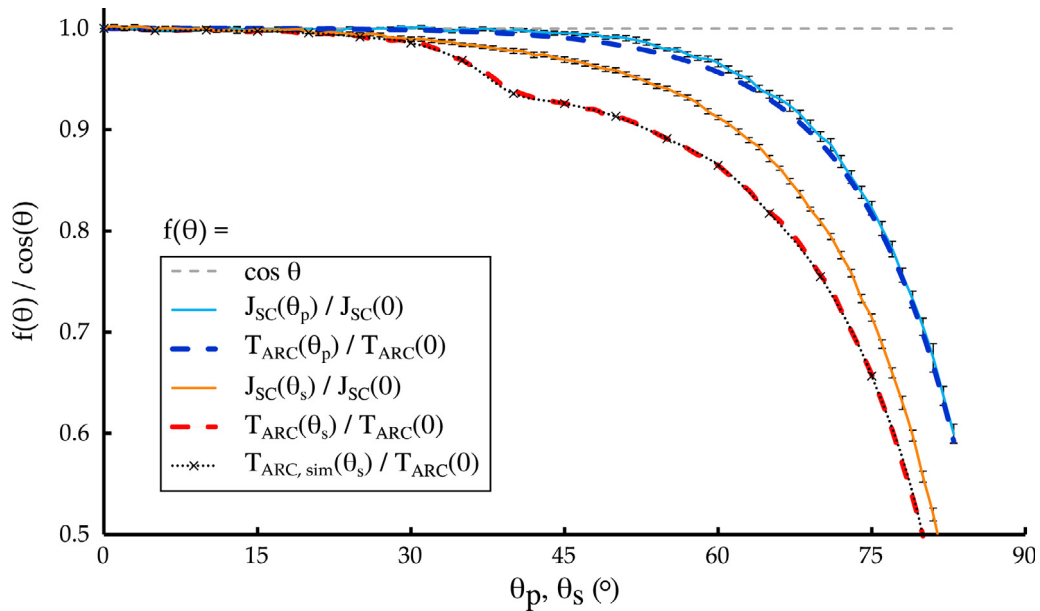


Fig. 6. Measured short circuit current densities and calculated/simulated transmission of light through the ARC as a function of θ_p and θ_s . All data is normalized to their value under normal incident light and divided by $\cos \theta$ to correct for the decreasing light intensity under inclined angles. The resp. measured J_{SC} values are represented in continuous lines by the average value over 6 separate datasets (3 different cells, 2 measurements per cell) with vertical bars showing the standard deviation. The dashed lines represent the transmission through the ARC based on Fresnel reflections, when reflections off the grid metal is respectively neglected (blue) or included (red). (For interpretation of the references to color in this figure legend, the reader is referred to the web version of this article.)

of the lens has only a single concentration wavelength (λ_c) for projection. λ_c which will be determined to produce the best performance for a given spectrum using Scientrace. The spectrum used in the simulations is derived from the NREL ASTM G-173 Direct + Circumsolar spectrum (NREL, 2012), and can be found in the Scientrace repository on Github (Bos-Coenraad, 2016).

Other factors influencing system performance are the angular aperture of the sun, and errors in the optical components and/or their alignment.

Instead of modeling roughnesses and errors of the optical components the angular aperture of the incident light (θ_x) at the Fresnel lens has been increased from the sunlights default of $\theta_x = \pm 0.25^\circ$ up to $\theta_x = \pm 0.75^\circ$.

4. Results and discussion

4.1. Electrical performance

As a part the J-V curve measurements, short circuit current densities for the AOI ranges θ_s and θ_p are obtained using four-terminal sensing. Averages for $N_{J_{SC}}(\theta_p)$ and $N_{J_{SC}}(\theta_s)$ over six separate measurement series are plotted with their standard deviations in Fig. 6. The obtained experimental data for $N_{J_{SC}}(\theta_p)$ (continuous blue line in Fig. 6) drops below 1 when $\theta \geq 35^\circ$, indicating a loss of performance in the solar cell efficiency for illumination angles exceeding this point. The deviation increases severely as the AOI increases further; up to an efficiency loss of 40% for AOI of 83° . In a first order

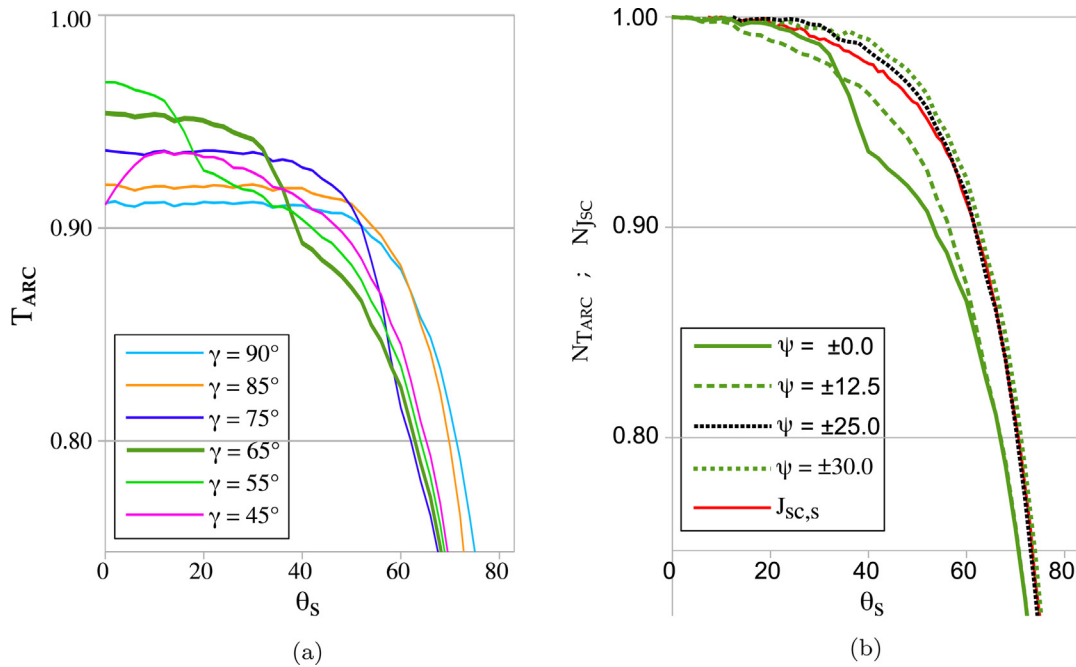


Fig. 7. (a) Transmission of light through the ARC for several grid finger slopes γ , as a function of the orthogonal incident angle (θ_s) as obtained by ray tracing simulations. (b) Normalized simulated transmissions and measured short circuit current density as a function of the orthogonal incident angle (θ_s) for several values of the scattering parameter ψ .

approximation of the amount of light actually entering the semiconductor volume, $N_{Jsc}(\theta_p)$ and the theoretical transmission through the ARC $N_{TARC}(\theta_p)$ (dashed blue line in Fig. 6) are compared. $N_{TARC}(\theta_p)$ is based on partial Fresnel reflections while reflections off the InGaP surface, and interference effects are neglected. A close overlap between the two curves is observed, indicating that the increased reflections at the ARC surface under oblique angles are the major cause of the noted efficiency loss.⁵

For $N_{Jsc}(\theta_s)$ (continuous orange line in Fig. 6) an even stronger efficiency loss of an additional 18% at 83° AOI is observed, and also it starts from a lower AOI of approximately 20° . In this case the incident light beam is oriented orthogonal to the inclined sides of the grid fingers as shown in Fig. 2. Therefore as AOI increases, an increasing fraction of light will fall on these side walls as opposed to directly on the ARC. Reflections off these inclined surfaces will cause this increasing fraction of light to reach the solar cell surface at an even more oblique angle, as is further detailed in Appendix B. The cumulative effects of an increasing fraction of light reaching the cell at angles steeper than the set AOI is a cause for the noted difference in cell efficiency for θ_p and θ_s illumination orientations. Yet when these effects are taken into account in the calculation of the theoretical transmission through the ARC for orthogonal beam orientation, $N_{TARC}(\theta_s)$ (dashed red line in Fig. 6), no satisfactory overlap with $N_{Jsc}(\theta_s)$ is found for AOI beyond 30° . The calculation displays a *fast drop* at this point that is not noted in the measurements. In these calculations the grid fingers were treated as perfect reflectors, and the *fast drop* occurs when the increasing fraction L_x enters the semiconductor surface at an incident angle of 80° . This increases to *horizontal* reflection (90°) at $\theta_s = 40^\circ$. At this point, this *fast drop* in the $N_{TARC}(\theta_s)$ curves ends, since $\alpha(\theta_s = 40^\circ) = 90^\circ$, hence the entire reflected fraction is lost

at $\theta_s \geq 40^\circ$. As is apparent, in a real solar cell these grid fingers will not be perfect mirrors.

4.2. Geometrical grid finger analysis

As shown in Fig. 6 the *fast drop* in $N_{TARC}(\theta_s)$ is absent in the measurements for $N_{Jsc}(\theta_s)$. Because in a real device the grid fingers are rough on a micrometre scale (see also Fig. 4), reflective scattering at the grid will take place. Here, we introduce this scattering into the analysis in an effort to explain the discrepancy between the calculated $N_{TARC}(\theta_s)$ and experimentally obtained $N_{Jsc}(\theta_s)$ values. As these analyses are too complex to perform analytically they are performed using 3D ray tracing simulations. To visualize the equivalence between the analytical calculations and ray tracing, results from simulations without scattering ($\psi = 0^\circ$) are included in Fig. 6 as $N_{TARC, sim}(\theta_s)$. This clearly shows that the results of the simulations perfectly match of the analytic calculations $N_{TARC}(\theta_s)$.

Fig. 7a shows the simulated normalized transmission $N_{TARC, sim}(\theta_s)$ for various grid finger slopes γ , as a function of θ_s . For increasing γ , the transmission at near normal incident irradiation (0 – 20°) decreases. That occurs because the light fractions L_x and L_y on the sides of the grid fingers, become smaller for increasing γ in favor of a larger fraction L_t on the top of the grid fingers, which is inherently lost. For $\gamma = 45^\circ$ the transmission first increases with θ_s before going through an optimum. This is explained as at this grid finger inclination, at $\theta_s = 0^\circ$ the entire light fractions L_x and L_y reflect horizontally and are lost, while for larger θ_s part of the reflection is pointed towards the cell surface. For $45^\circ \leq \gamma \leq 90^\circ$ all normalized transmission curves show the previously discussed *fast drop*. With increasing γ the *fast drop* occurs at higher θ_s and becomes less pronounced as it occurs at an increasingly steeper part of the curve. Again, the location signifies the AOI for which L_x undergoes horizontal reflection with respect to the cell surface and is therefore lost.

The studied concentrator solar cells have grid lines with $\gamma = 65^\circ$. In Fig. 7b normalized transmission simulations for a solar

⁵ Note that the cells under test are equipped with an ARC for use with a glass SOE while measured in air. However if a glass cover or SOE is placed in front of the cell, similar Fresnel reflections would occur on the air-glass interface, yielding similar loss of performance in the solar cell.

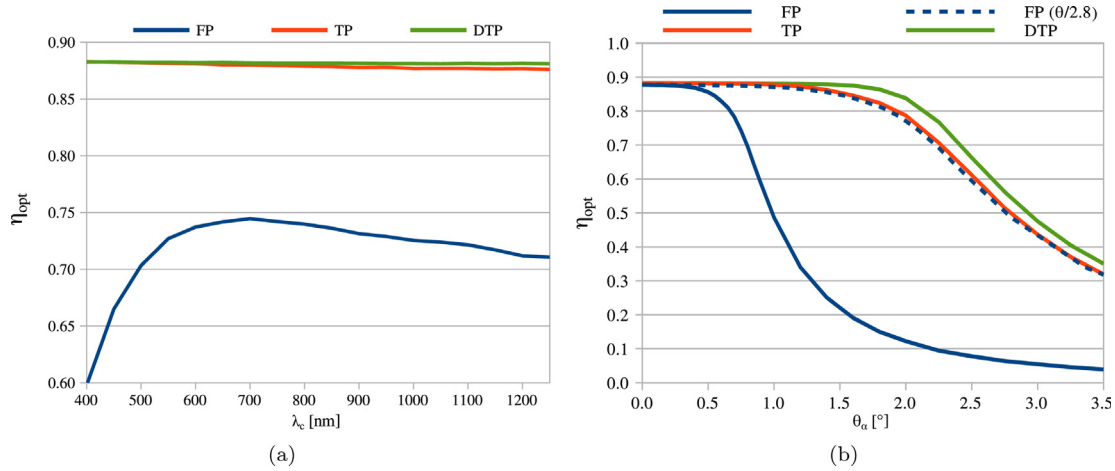


Fig. 8. (a) The optical efficiency (η_{opt}) with the different SOEs as a function of the lens concentration wavelength (λ_c). Dispersion of the incident AM1.5 spectrum by the PMMA Fresnel lens causes the focal point to shift as a function of the wavelength. Here, the focal point is always kept at the top of the SOE. Additional losses are due to the angular aperture of the incident light of $\pm 0.75^\circ$ and partial reflections at the lens ($2\times$) and SOEs ($1\times$). (b) η_{opt} as a function of the angular aperture (θ_a) of the incident light for different SOE's. The dashed line shows the value of the FP plot where η_{opt} is plotted against $\theta_a/2.8$, suggesting a virtually increased acceptance angle of $2.8\times$.

cell with this grid configuration are compared to the experimentally obtained $N_{Jsc}(\theta_s)$. Each curve represents a different degree of scattered reflections at the grid metal, quantified by ψ as described in Section 3.3. The figure shows that the introduction of scattered reflections smooths out the AOI dependent transmission curve, rapidly eliminating the *fast drop*.

For $\psi = 25^\circ$ the simulated transmission closely matches the experimentally obtained $N_{Jsc}(\theta_s)$ data, indicating that the observed differences between $J_{sc}(\theta_s)$ and $J_{sc}(\theta_p)$ can be fully explained by scattered reflection from the sloping sides of the gridfingers. Fig. 7 also shows that enhanced scattering is beneficial for the transmission of light to the solar cell as it salvages part of the increasing fraction of light that would otherwise reflect away from the solar cell for oblique illumination angles.

4.3. SOE ray tracing simulations

The optical properties of three model secondary optics have been investigated, in order to compare the benefit of using a SOE to the introduced loss of performance caused by the increased average illumination angle of the solar cell. The optical efficiency η_{opt} of the SOE concentrator models is determined for the AM1.5 spectrum as a function of the concentration wavelength (λ_c , Fig. 8a) using Scientrace. This analysis shows that the FP model is most susceptible to dispersion related losses, while the concentrating SOEs (TP and DTP) are barely influenced. In favor of the short wavelength photons in the spectrum, that are usually limiting the performance of concentrator solar cells, and as a compromise for all SOE models, λ_c is defined at 650 nm in all of the following simulations. The benefit of the concentrating SOEs is also illustrated by Fig. 8b where η_{opt} is determined as a function of the angular aperture of the incident light. The TP and DTP SOEs still are able to function well at lesser beam qualities.

The dashed line shows that when a FP is employed, in order to reach a similar optical efficiency⁶ as when using a TP SOE, the angular aperture should be reduced by a factor of 2.8. A very similar result has been found for a Compound Parabolic Concentrator (CPC) by Victoria et al. as plotted in their figure 2 Victoria et al. (2009). Although the TP and the CPC have different base geometries, in many aspects they behave similar. It should be noted that the *acceptance angle* described in the referred study is not the same as the *angular aper-*

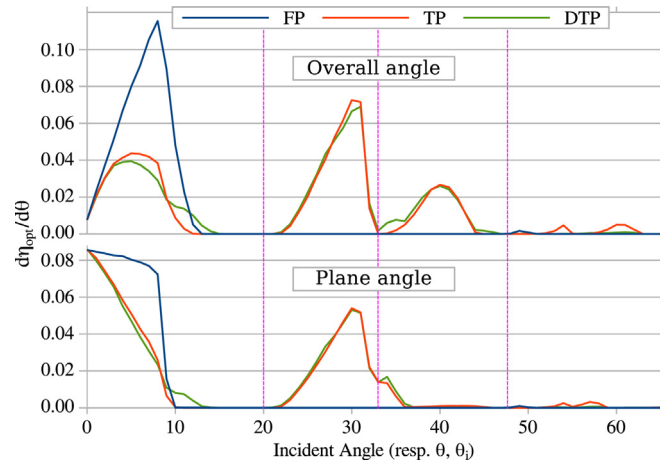


Fig. 9. The angular optical efficiency, $d\eta_{opt}/d\theta$, as a function of θ and θ_p for the basic concentrator model (standard conditions: $\theta_a = \pm 0.75^\circ$, $\lambda_c = 650$ nm). The top figure plots the angular optical efficiency against the 'overall incident angle', whereas the bottom figure uses the incident angle decomposed in 'plane angles' θ_p and θ_s . The pink lines separate different incident angle ranges. (For interpretation of the references to color in this figure legend, the reader is referred to the web version of this article.)

ture in this study, but both variables can readily be used to describe the sensitivity/robustness of the optical system. In addition, the referred simulation does not include dispersion effects from the primary optics nor do the dimensions of the used optics match. Despite these differences in setup, the improvement of the system by both SOEs show clear similarities. For the CPC optic an increase in angular transmission by a factor of 3.33 was found for 90% optical efficiency, and 2.85 for 80% optical efficiency, compared to a steady increase of a factor 2.8 for the TP optic in the current study.

Fig. 9 shows the optical efficiency of light on the solar cell as a function of the incidence angle for the three SOE configurations. As such, it reflects the distribution of AOIs for incident photons for each configuration, and shows how the use of the SOEs alters the AOI distribution at the cell surface. Here, the "overall angle" represents θ for a photon incident at the cell surface regardless of its orientation ϕ . Conversely in the "plane angle" graph θ is deconvoluted into its projections θ_p and θ_s . Due to rotational symmetry in the studied SOEs, these distributions overlap completely. The figure shows that while for the FP system θ remains

⁶ η_{opt} , the fraction of the light that is emitted to reach the surface of the solar cell, cell reflection and performance are excluded.

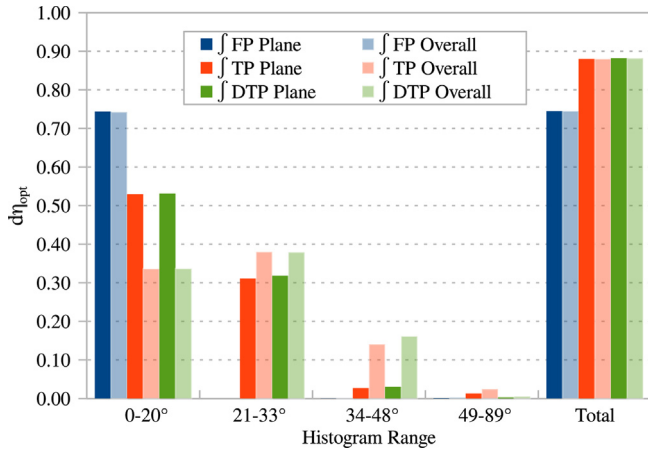


Fig. 10. The optical efficiency integrated over the ranges as denoted in Fig. 9, showing both the 'overall angle' integrals and those of the 'plane angle' decompositions.

at near-normal incidence, for the TP and DTP configurations the average θ increases as light incident at the cell surface in the 20–50° range is introduced. Note that θ in the 20–30° range arise due to a single internal reflection in the SOE, while higher values of θ are caused by two or more internal reflections. Therefore the angular distributions are integrated for these intervals separately and shown in Fig. 10. Here, we show that although the average AOI is greatly increased when a SOE is employed, this is offset by an increase in optical efficiency exceeding 10%. However, it should be considered that 30° angle in a BK7 medium ($n \approx 1.5$) equals a 49° angle in vacuum ($n = 1.0$), whereas 40° in BK7 equals 75° in vacuum ($\alpha_{vac} = \sin^{-1} n_{BK7} \alpha_{BK7}$). Especially for the latter, grid orientation related losses can become over 10%. Therefore if an asymmetric CPV system (Voarino et al., 2014) is being considered, or inhomogeneous primary optic illumination is expected (Bunthof et al., 2016), this effect should be taken into account. For instance when using a regular straight grid the cell should be oriented carefully with respect to the optics to minimize these grid-induced optical losses. Alternatively, more advanced grid patterns may also provide a way to minimize these effects (Bissels et al., 2011).

5. Conclusions

Using the normalized current density as a parameter, the electrical performance of TJ CPV solar cells for varying angles of incident illumination has been studied in detail. While the λ in $EQE(\lambda, \theta)$ (Eq. 4) is almost entirely related to semiconductor properties, this study shows that θ can be explained almost entirely by the ARC and the grid contact configuration and morphology. During experimental testing, the solar cells perform considerably, and increasingly worse as illumination becomes more oblique. A performance reduction of up to 58% has been determined for an AOI of 83°. This loss of performance is mainly attributed to the optical properties of the ARC because calculated AOI dependent transmission through this coating correlates excellently with the observed AOI dependent cell performance. A second loss mechanism has been identified and attributed to the front contact grid by propagating the AOI orthogonal to the grid fingers. In this case an increasing fraction of illumination will interact with the sides of the grid metal for increasing AOI. Therefore the specific shape and orientation of the grid fingers become an increasingly important source of cell performance loss for oblique illumination. As a consequence, an additional loss in current generation of up to 18% has been attributed to the front grid. This loss of performance cannot be fully explained by increased Fresnel reflections off the ARC for

the fraction of incident light that reflects off the grid. Ray tracing simulations however, demonstrated that the additional loss in electrical performance can be fully explained by scattered reflections off the grid fingers, which were shown to exhibit a rough surface on a microscopic scale. Because of this, the electrical losses in the solar cell at oblique angles would actually be higher if the sides of the grid fingers are perfectly smooth.

The optical properties of three model SOEs have been investigated, in order to compare the benefit of using a SOE, to the introduced loss of performance caused by the increased average illumination angle of the solar cell. The optical efficiency of the system as a function of photon wavelength has been shown to be significantly higher for the studied truncated pyramid SOEs compared to a flat glass plate, with more than 15% absolute increase in optical efficiency for each wavelength. Also a strong increase in angular acceptance of a factor of 2.8 has been shown for the TP SOEs. On the other hand the SOEs introduce illumination angles in the 20–50° range, while simultaneously diminishing the fraction of near-normal (0–10°) illumination compared to the glass plate. When all three of these factors are taken into account, both TP and DTP SOEs display an optical efficiency that exceeds that of the glass plate by more than 10%, which clearly illustrates the benefit of using a SOE in a lens based CPV system. In the current study this was demonstrated for a system with a circular Fresnel lens primary optic, and SOEs that have 90° rotational symmetry. In CPV systems where either optic is not symmetric (i.e. parabolic trough and/or prism based systems) however, the performance diminishing effect of the non-normal illumination may be greater due to the influence of the front grid as demonstrated in this work. Therefore grid orientation or design with respect to the optical system should be taken into account and optimized in such systems.

Acknowledgements

The authors acknowledge European Commission's FP7 and the Netherlands Enterprise Agency for financial support for this project through grant agreement ENER/FP7/296014/“CPV4ALL”, and project TKIZ01019, respectively.

Appendix A. Refractive indices for simulated volumes

The photon wavelength ($\lambda_{\mu m}$) is defined in micrometers for these equations.

A.1. Poly(methyl methacrylate), PMMA

$$n = 1.478 + \frac{4.53 \cdot 10^{-2}}{\lambda_{\mu m}^2}$$

A.2. BK7 glass

$$n^2 - 1 = \frac{1.03961212 \lambda_{\mu m}^2}{\lambda_{\mu m}^2 - 0.00600069867} + \frac{0.231792344 \lambda_{\mu m}^2}{\lambda_{\mu m}^2 - 0.0200179144} + \frac{1.01046945 \lambda_{\mu m}^2}{\lambda_{\mu m}^2 - 103.560653}$$

(insert BK7 bibtex-ref <http://refractiveindex.info/?shelf=glass&book=BK7&page=SCHOTT>).

Appendix B. Calculation of orthogonal incident transmission

The surfaces l_x and l_y are virtually shadowed/reflected by the grid finger slopes:

$$l_\theta = h \tan(\theta_s), \quad l_\gamma = \frac{h}{\tan(\gamma)}$$

$$l_x = \begin{cases} l_\gamma + l_\theta, & \text{if } l_\gamma + l_\theta < l - l_t \\ l - l_t, & \text{otherwise} \end{cases} \quad (\text{B.1})$$

$$l_\beta = \begin{cases} l_\gamma - l_\theta, & \text{if } \theta_s + \gamma < 90^\circ \\ 0, & \text{otherwise} \end{cases} \quad (\text{B.2})$$

The incident angles with the semiconductor surface normal after geometric reflections upon the grid sides:

$$\beta = 180^\circ - \theta_s - 2\gamma \quad (\text{B.3})$$

$$\alpha = 180^\circ + \theta_s - 2\gamma \quad (\text{B.4})$$

The length of the semiconductor area in between the grid fingers that is directly irradiated:

$$l_s = l - (l_t + l_x + l_\beta) \quad (\text{B.5})$$

The total orthogonal transmission based on the incident fractions and the resp. cold ARC transmissions:

$$T_{\text{ARC},s}(\theta_s) \equiv \frac{l_s}{l} T_{\text{ARC}}(\theta_s) + \frac{l_x}{l} T_{\text{ARC}}(\alpha) + \frac{l_\beta}{l} T_{\text{ARC}}(\beta) \quad (\text{B.6})$$

References

- Antón, I., Pachón, D., Sala, G., 2003. Characterization of optical collectors for concentration photovoltaic applications. *Prog. Photovoltaics* 11 (6), 387–406.
- Baharoon, D.A., Rahman, H.A., Omar, W.Z.W., Fadhl, S.O., 2015. Historical development of concentrating solar power technologies to generate clean electricity efficiently—a review. *Renew. Sustain. Energy Rev.* 41, 996–1027.
- Benitez, P., Miñano, J., 2003. Concentrator optics for the next-generation photovoltaics. *Next Gener. Photovoltaics*, 285.
- Benítez, P., Miñano, J.C., Zamora, P., Mohedano, R., Cvetkovic, A., Buljan, M., Chaves, J., Hernández, M., 2010. High performance fresnel-based photovoltaic concentrator. *Opt. Express* 18 (101), A25–A40.
- Bissels, G.M.M.W., Asselbergs, M.A.H., Schermer, J.J., Haverkamp, E.J., Smeenk, N.J., Vlieg, E., 2011. A genuine circular contact grid pattern for solar cells. *Prog. Photovoltaics Res. Appl.* 19 (5), 517–526.
- Bos-Coenraad, J., 30-March-2016. Scientrace Spectrum XML File, Based on the AM1.5 G-173 Data by NREL. <https://github.com/JoepBC/scientrace/blob/master/spectrum_am1.5/astmg173-direct-300-1800nm-res10nm.scx-spectrum>.
- Bunthof, L.A.A., Kreuwel, F.P.M., Kaldenhoven, A., Kin, S., Corbeek, W.H.M., Bauhuis, G.J., Vlieg, E., Schermer, J.J., 2016. Impact of shading on a flat CPV system for façade integration. *Sol. Energy* 140, 162–170.
- Dumeige, Y., Sagnes, I., Monnier, P., Vidakovic, P., Abram, I., Mériadec, C., Levenson, A., 2002. Phase-matched frequency doubling at photonic band edges: efficiency scaling as the fifth power of the length. *Phys. Rev. Lett.* 89 (4), 043901.
- Espinete González, P., Mohedano, R., García Vara, I., Zamora Herranz, P., Rey-Stolle Prado, I., Benítez Gimenez, P., Algorta del Valle, C., Cvetkovic, A., Hernández Sanz, M., Chaves, J., et al., 2012. Triple-junction solar cell performance under fresnel-based concentrators taking into account chromatic aberration and off-axis operation. In: *Conference Proceedings*.
- Fernández, E.F., Higuera, P.J.P., Siefer, G., et al., 2011. Monolithic III-V triple-junction solar cells under different temperatures and spectra. In: *2011 Spanish Conference on Electron Devices (CDE)*. IEEE, pp. 1–4.
- Fiore, A., Berger, V., Rosencher, E., Bravetti, P., Nagle, J., 1998. Phase matching using an isotropic nonlinear optical material. *Nature* 391 (6666), 463–466.
- García, I., Algorta, C., Rey-Stolle, I., Galiana, B., 2008. Study of non-uniform light profiles on high concentration III-V solar cells using quasi-3d distributed models. In: *Photovoltaic Specialists Conference, 2008. PVSC'08. 33rd IEEE*. IEEE, pp. 1–6.
- García-Linares, P., Domínguez, C., Voarino, P., Besson, P., Baudrit, M., 2014. Effect of the encapsulant temperature on the angular and spectral response of multi-junction solar cells. In: *2014 IEEE 40th Photovoltaic Specialist Conference (PVSC)*. IEEE, pp. 3298–3303.
- Herrero, R., Victoria, M., Domínguez, C., Askins, S., Antón, I., Sala, G., 2012. Concentration photovoltaic optical system irradiance distribution measurements and its effect on multi-junction solar cells. *Prog. Photovoltaics Res. Appl.* 20 (4), 423–430.
- James, L.W., 1989. Use of Imaging Refractive Secondaries in Photovoltaic Concentrators. SAND89-7029, Albuquerque, New Mexico.
- James, L.W., 1994. Effects of concentrator chromatic aberration on multi-junction cells. *Photovoltaic Energy Conversion, 1994., Conference Record of the Twenty Fourth. IEEE Photovoltaic Specialists Conference-1994, 1994 IEEE First World Conference on*, vol. 2. IEEE, pp. 1799–1802.
- Jaus, J., Peharz, G., Gombert, A., Rodriguez, J.P.F., Dimroth, F., Eltermann, F., Wolf, O., Passig, M., Siefert, G., Hakenjos, A., et al., 2009. Development of FLATCON® modules using secondary optics. In: *Photovoltaic Specialists Conference (PVSC), 2009 34th IEEE*. IEEE, pp. 001931–001936.
- Kinsey, G.S., Hebert, P., Barbour, K.E., Krut, D.D., Cotal, H.L., Sherif, R.A., 2008. Concentrator multijunction solar cell characteristics under variable intensity and temperature. *Prog. Photovoltaics Res. Appl.* 16 (6), 503–508.
- Martin, Y., Kirchner, P.D., van Kessel, T., Wacaser, B., Sandstrom, R., Patel, D., Kim, B., Badahdah, A., Khonkar, H., Leutz, R., 2015. High-concentration photovoltaics effect of inhomogeneous spectral irradiation. *IEEE J. Photovoltaics* 5 (1), 454–460.
- Mohedano, R., Leutz, R., 2016. CPV optics. *Handbook Concentrator Photovoltaic Technol.*, 207.
- NREL, 2012. Reference Solar Spectral Irradiance: ASTM G-173. <<http://rredc.nrel.gov/solar/spectra/am1.5/astmg173/astmg173.html>> (accessed 9-May-2016).
- NREL, 2016. Best Research-Cell Efficiencies. <http://www.nrel.gov/ncpv/images/efficiency_chart.jpg> (accessed 12-January-2016).
- Or, A.B., Appelbaum, J., 2014. Dependence of multi-junction solar cells parameters on concentration and temperature. *Sol. Energy Mater. Sol. Cells* 130, 234–240.
- Rodrigo, P., Fernández, E.F., Almonacid, F., Pérez-Higuera, P., 2013. Outdoor measurement of high concentration photovoltaic receivers operating with partial shading on the primary optics. *Energy* 61, 583–588.
- Schmid, T., Wiesenfarth, M., Hornung, T., Gremmelspacher, M., Manns, P., Nitz, P., 2014. Mass manufactured secondary optics for CPV. *10th International Conference on Concentrator Photovoltaic Systems: CPV-10*, vol. 1616. AIP Publishing, pp. 84–87.
- Swanson, R.M., 2000. The promise of concentrators. *Prog. Photovoltaics Res. Appl.* 8 (1), 93–111.
- Victoria, M., Domínguez, C., Antón, I., Sala, G., 2009. Comparative analysis of different secondary optical elements for aspheric primary lenses. *Opt. Express* 17 (8), 6487–6492.
- Voarino, P., Domínguez, C., Bijl, R., Penning, P., 2014. Optical performance analysis of a novel tracking-integrated concentrator through ray tracing. *10th International Conference on Concentrator Photovoltaic Systems: CPV-10*, vol. 1616. AIP Publishing, pp. 215–219.
- Welford, W., 1977. Optical estimation of statistics of surface roughness from light scattering measurements. *Opt. Quant. Electron.* 9 (4), 269–287.